Solubility of gold in arsenian pyrite

MARTIN REICH,[1,2,*] STEPHEN E. KESLER,[1] SATOSHI UTSUNOMIYA,[1] CHRISTOPHER S. PALENIK,[1,3] STEPHEN L. CHRYSSOULIS,[4] AND RODNEY C. EWING[1]

[1]Department of Geological Sciences, University of Michigan, Ann Arbor, MI 48109-1063, USA
[2]Departamento de Geología, Facultad de Ciencias Físicas y Matemáticas, Universidad de Chile, Santiago, Chile
[3]Microtrace, 1750 Grandstand Place, Elgin, IL 60123, USA
[4]Advanced Mineral Technology Laboratory (AMTEL), London, Ontario, Canada

Abstract—Although Au and As can be enriched up to the weight percent level in arsenian pyrite, there is little knowledge of their limiting concentrations and nature of incorporation. This study reports SIMS and EMPA analyses showing that As and Au contents of arsenian pyrites plot in a wedge-shaped zone with an upper compositional limit defined by the line

$$C_{Au} = 0.02 \cdot C_{As} + 4 \times 10^{-5}$$

indicating a maximum Au/As molar ratio of ~0.02. Arsenian pyrites with Au/As ratios plotting above this limit contain nanoparticles of native Au, as observed by HRTEM imaging/EDS analysis and SIMS depth profiling. In this case, a significant amount of the total Au is present in its elemental form. In arsenian pyrites with Au/As < 0.02, native Au nanoparticles were not observed by HRTEM, and all of the Au measured is inferred to be structurally bound in solid solution. The microanalytical results, coupled with previously published XANES-EXAFS spectroscopic measurements confirm that arsenian pyrite compositions plotting above this limit contains Au^0, whereas arsenian pyrite compositions plotting below the limit contain Au^{+1}. On the basis of these observations, the upper bound is interpreted to represent a solubility limit for solid solution of Au as a function of As in arsenian pyrite between ~150°C and ~250°C, the approximate conditions under which samples used in the study were deposited. The Au-As composition of arsenian pyrite relative to this limit can be used to predict the chemical state of Au as well as the saturation state of Au in the hydrothermal solution that deposited it. These observations confirm that the parent hydrothermal solutions for the giant Carlin-type deposits, where solid solution of Au is dominant in arsenian pyrite, were largely unsaturated with respect to Au^0.

1. INTRODUCTION

Arsenic-rich pyrite, $Fe(S,As)_2$, commonly called "arsenian pyrite," contains ppm to weight-percent amounts of As and smaller but important amounts of Au and other trace metals such as Sb, Hg, Ni, Co, Cu, Tl, Ag, Zn, W, U, Pb, Bi, Se, and Te (Cook and Chryssoulis, 1990; Fleet et al., 1989, 1993, 1997; Arehart et al., 1993; Savage et al., 2000; Cline, 2001; Cline et al., 2003; Emsbo et al., 2003). Arsenian pyrite is found in numerous geologic settings, from sedimentary basins to hydrothermal ore deposits, including Carlin-type and epithermal Au deposits (Wells and Mullen, 1973; MacLean and Fleet, 1989; Cook and Chryssoulis, 1990; Richards and Kerrich, 1993; Savage et al., 2000; Kolker et al., 2003). Apart from being an economically important host for Au, arsenian pyrite is of great environmental interest because its oxidative dissolution can release significant amounts of As and trace metals into the environment (Savage et al., 2000; Sidle et al., 2001; Kolker et al., 2003).

During the last three decades, numerous studies have recognized a close association between Au and As in arsenian pyrite, and high-resolution analytical and spectroscopic measurements have shown that Au is present as both solid solution (Au^{+1}) and nanoparticles (Au^0) (Bakken et al., 1989; Cook and Chryssoulis, 1990; Fleet et al., 1993; Arehart et al., 1993; Sha, 1993; Friedl et al., 1995; Aylmore, 1995; Simon, 1998; Simon et al., 1999a, b; Savage et al., 2000; Cline, 2001; Ye, 2001; Emsbo et al., 2003; Palenik et al., 2004). Despite these advances, information is lacking on the maximum amount of Au that can be accommodated by arsenian pyrite and on how this limit is related to the occurrence of two forms of Au.

In Carlin-type deposits, where arsenian pyrite has been studied most intensively, a compilation of previously published Au-As SIMS and EMPA analyses (Fig. 1) shows that almost all data points fall within a wedge-shaped zone in log (Au)–log (As) space, which is limited by a relatively sharp boundary. Although available information on the chemical state of Au in arsenian pyrite is limited, the incorporation of XANES-EXAFS measurements from Simon et al. (1999a, b) into Figure 1 suggests that the occurrence of Au^{+1} and Au^0 may be related to different maximum Au-As contents.

In this study, we report additional secondary ionization mass spectrometry (SIMS) and electron microprobe analyzer (EMPA) measurements and high-resolution transmission electron microscopy (HRTEM) observations that define limits for the solubility and chemical state of Au in arsenian pyrite. When coupled with previously published analytical and spectroscopic information, these data show that the maximum contents of Au are constrained by a solubility limit that controls the occurrence of solid solution (Au^{+1}) and nanoparticulate (Au^0) Au in arsenian pyrite. Finally, this study documents how this solubility limit can be used to predict the chemical state of Au in arsenian

* Author to whom correspondence should be addressed (mreichm@umich.edu).

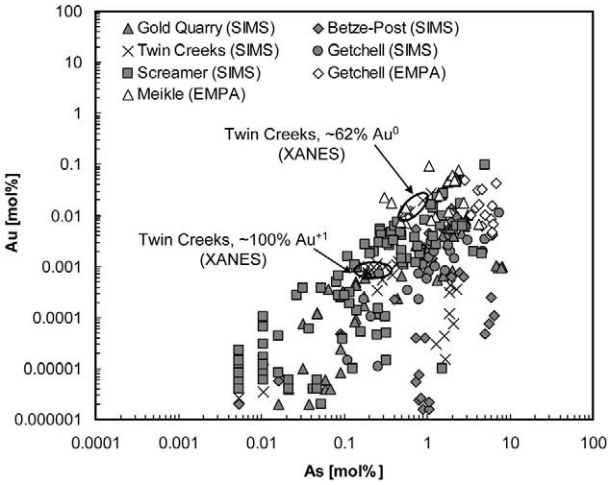

Fig. 1. Plot of previously published Au-As SIMS and EMPA analyses of arsenian pyrite from Carlin-type deposits. Sources of data: Arehart et al. (1993) for Betze-Post, Sha (1993) for Gold Quarry, Simon et al. (1999b) for Twin Creeks, Cline (2001) for Getchell, Ye (2001) for Screamer, and Emsbo et al. (2003) for Meikle. XANES-EXAFS spectroscopic data for arsenian pyrite samples from Twin Creeks (CTW150/898: Au^{+1}~100%; and CTW12/822: Au^{0} ~62%) were taken from Simon et al. (1999a).

pyrite and consequently evaluate the saturation state of hydrothermal solutions with respect to native Au.

2. PREVIOUS EXPERIMENTAL AND ANALYTICAL STUDIES

The solubility of Au in nonarsenian (pure) pyrite is very low (a few ppm), and values greater than 100 ppm are usually associated with As-rich compositions (Cook and Chryssoulis, 1990). Whereas Tauson (1998, 1999) obtained a solubility of 3 ± 1 ppm Au in pyrite at 500°C and 1 kbar, numerous investigators have shown that high Au contents are always correlated with As-rich compositions in natural and synthesized pyrites (Wells and Mullen, 1973; Sha, 1993; Arehart et al., 1993; Fleet and Mumin, 1997; Simon et al., 1999b; Cline, 2001; Pals et al., 2003). *Ab initio* quantum mechanical calculations by Reich et al. (2003) support these observations. At the atomic scale, results show that the total energy of the auriferous arsenian pyrite lattice varies with respect to the Au-As atomic distance. Configurations in which As atoms are clustered around an Au atom are more energetically favorable than those in which an Au atom is in far vicinity to As atoms. Despite a dependence of Au upon As, as is observed in arsenian pyrite, the inverse relation is not true. As-rich, Au-poor pyrites are found in a variety of geological environments and are an important source for As dispersion into soils and groundwaters (Savage et al., 2000; Sidle et al., 2001; Kolker et al., 2003; Utsunomiya et al., 2003).

Au-bearing arsenian pyrite can exhibit several different textural types. For example, in Carlin-type deposits arsenian pyrite is present as small (<4 μm) anhedral grains or thin (<5–10 μm) overgrowths on preexisting coarser-grained pyrite crystals (Wells and Mullen, 1973). Au is associated exclusively with As-rich growth bands in these fine rims, and SIMS analyses show a positive correlation between Au and As (Wells and Mullens, 1973; Radtke, 1985; Cook and Chryssoulis, 1990; Fleet et al., 1993; Arehart et al., 1993; Sha, 1993; Pals et al., 2003). Two mineralogic forms of Au have been described in the rims: structurally bound (solid solution) and submicron inclusions (nanoparticles) of native Au. Although early EMPA and SEM studies suggested the presence of both types of Au (Radtke et al., 1972; Wells and Muellens, 1973), it was not until 1989 that submicron-sized (5–20 nm) Au particles were imaged using HRTEM (Bakken et al., 1989). X-ray absorption near-edge structure (XANES) and extended x-ray absorption fine structure (EXAFS) measurements by Simon et al. (1999a) confirmed the presence of the two forms of Au (Au^{0} and Au^{+1}) in arsenian pyrite. Au^{0} was attributed to submicron-sized native Au particles that do not occupy a structural position in arsenian pyrite, whereas Au^{+1} was attributed to Au in the lattice of arsenian pyrite.

SIMS, EMPA, and XANES-EXAFS studies have confirmed that As substitutes for S in pyrite (Cook and Chryssoulis, 1990; Simon et al., 1999a; Savage et al., 2000). However, the structural position and substitutional mechanisms for Au in the arsenian pyrite are still not well understood. EMPA analyses of arsenian pyrite from the Deep Star deposit in Nevada revealed an apparent negative correlation between Au and Fe, leading to the conclusion that high concentrations of invisible Au correlate with a deficiency of Fe (Fleet and Mumin, 1997). Specific information about the possible location of Au in the pyrite structure has been provided by spectroscopic studies. Friedl et al. (1995), using Mössbauer spectroscopy and the analogy of substitutions in PtX_2 compounds (chalcogenides and pnictides), suggested that Au replaces Fe in the pyrite lattice, being octahedrally coordinated by six S. The XANES-EXAFS results of Simon et al. (1999a) provide a more detailed description of the coordination environment for solid-solution Au in arsenian pyrite. Two coordination numbers (2 and 4) for Au^{+1} in arsenian pyrite were deduced from XANES and EXAFS spectra. Under this scheme, Au^{+1} would be linearly coordinated with two sulfide ligands (twofold coordination), although the available information does not allow the discrimination between three alternative forms of fourfold coordination (Au^{+1} in a distorted octahedral site, in a vacancy, or in an unknown Au-As-S compound).

The pressure-temperature stability (or metastability) range of As-bearing pyrite still remains unresolved, although prevailing opinion holds that it is metastable at all P-T. Crystallization of pyrite, marcasite, and arsenopyrite at low temperatures (<300°C) is dependent on the reaction path (Murowchick and Barnes, 1986; Wu and Delbove, 1989; Schoonen and Barnes, 1991a, b, c; Pokrovski et al., 2002). Experimental studies by Fleet et al. (1989) and Fleet and Mumin (1997) have revealed a widespread metastable persistence of solid solutions along the FeS_2-FeAsS join, although the maximum solubility limit of As in pyrite has not been determined experimentally. Clark (1960) obtained 0.53 wt.% As at 600°C in dry experiments in the Fe-As-S system and concluded that very little As is soluble in pyrite. Notwithstanding, wet experimental studies by Kretschmar and Scott (1976) and hydrothermal synthesis by Fleet and Mumin (1997) documented much higher maximum As contents in pyrite (7.9 wt.% As in the assemblage py+As+liq+vap at 400°C, and 9.3 wt.% As in metastable As-rich pyrite (Fe-*S*-As-Au system) between 300°C and 500°C, 1.3–1.6 kbar, respectively).

3. SAMPLES AND METHODS

3.1. Samples

Au-bearing arsenian pyrite grains and overgrowths from Carlin-type deposits in Nevada (Screamer, Meikle, Deep Star, and Lower Post) were studied using EMPA, SIMS, and HRTEM techniques. For a detailed description of the geology of these deposits, the reader is referred to Ye et al. (2003), Emsbo et al. (2003), Heitt et al. (2003), and Leach (1993), respectively. Additional EMPA and SIMS analyses were carried out on arsenian pyrite samples from epithermal Au deposits at Porgera (Papua New Guinea), Mule Canyon (Nevada), and Kirazli (Turkey). Geologic information on these deposits can be found in Richards and Kerrich (1993) and John et al. (2003). In addition to our analytical results, we have compiled previously published SIMS and EMPA Au-As analyses of arsenian pyrite from Carlin-type deposits in Nevada. EMPA analyses were taken from Emsbo at al. (2003) for Meikle and Cline (2001) for Getchell. SIMS analyses were taken from Sha (1993) for Gold Quarry, Arehart et al. (1993) for Betze-Post, Simon et al. (1999b) for Twin Creeks, and Cline (2001) for Getchell. Additional SIMS analyses from the Emperor epithermal Au deposit in Fiji were taken from Pals et al. (2003).

3.2. EMPA, SIMS, and HRTEM Techniques

The composition of arsenian pyrite samples was measured using EMPA and SIMS as complementary techniques, because neither can obtain a small sample volume and a low detection limit simultaneously. SIMS is currently one of the most sensitive microbeam techniques available for detecting ppm concentrations of Au, with detection limits as low as 0.4 ppm Au and an accuracy of ~10%–~15% (Chryssoulis et al., 1987, 2004). However, the diameter of the SIMS beam (~10–~20 μm) limits the analysis of small grains and thin overgrowths (<20 μm). This difficulty can be overcome by using EMPA, which has a smaller electron beam diameter under static conditions (~2 μm) and can resolve smaller sample volumes (~10 μm^3). Unfortunately, the detection limit for Au under normal operating conditions of EMPA is high (several tenths of a wt.% level for routine analyses), although it can be lowered to several hundred ppm by increasing the accelerating voltage, beam current and/or counting times.

EMPA measurements of samples from the Screamer, Meikle, Deep Star, and Porgera deposits were performed at the University of Michigan Electron Microbeam Analysis Laboratory (EMAL) using a CAMECA SX100 with five x-ray Wavelength Dispersive Spectrometers (WDS). Arsenian pyrite was analyzed for Fe (Kα), S (Kα), As (Lα), Au (Mα), Sb (Lβ), Hg (Mα), Ni (Kα), Te (Lα), Se (Lα), and Co (Kα). The following sulfides and native metals were used as standards: FeS_2 (Fe, S), FeAsS (As), Au^0 (Au), Sb_2S_3 (Sb), HgS (Hg), NiS (Ni), Te (SbTe), Se^0 (Se), and CoS (Co). Using a tight pulse height analysis (PHA) setting, no third-order WDS interference between Fe Kα and Au Mα lines was observed during pure pyrite (FeS_2) standard measurement. Microbeam analyses were done on coarse arsenian pyrite overgrowths (~5–~15 μm), to avoid signal contributions from minerals surrounding the grains. Beam damage of arsenian pyrite rims was minimal at operating conditions between 15 and 25 kV acceleration voltage and 10–40 nA intensity, keeping 120-s counting times for Au detection. The minimum detection limit of Au in arsenian pyrite under these conditions is ~250–~350 ppm.

SIMS analyses of samples from Lower Post, Mule Canyon, and Kirazli were performed using a Cameca IMS-3f ion microprobe (SIMS) at Advanced Mineral Technology Laboratory (AMTEL), London, Ontario. The measurements were done using a primary Cs^+ beam source of ~50–~55 nA at 14.5 keV, with 20 μm primary beam diameter and depth of analysis up to 1.2 μm. Energy filtering (by offsetting –180 V) was used to eliminate the isobaric interference from $^{133}Cs^{32}S_2$ and $^{58}Fe^{75}As^{32}S_2$ on ^{197}Au. Under these conditions the background signal at 197 Daltons, due to the $^{133}Cs^{32}S_2$ isobaric interference, corresponds to an Au concentration of 0.24 ppmw (parts-per-million by weight) (Fig. 2). This background for pyrite varies very little (±0.02 ppm Au), so for low Au concentrations in pyrite (<1 ppm) the background is subtracted to obtain a more accurate measurement of Au concentration. Calibration of Au and As was done by external standarization using pyrite implanted with Au and As (Chryssoulis et al., 1989). The minimum detection limits for Au and As were 150 and 500 ppb, respectively, at the 2σ level. The dynamic mode of the SIMS analysis, whereby successively deeper layers are analyzed with time, enables the detection of submicron Au inclusions from the sudden change in the Au signal intensity between layers (Chryssoulis, 1990). In SIMS depth profiles, Au nanoinclusions are registered as spikes on a background of solid-solution Au, and the minimum size detectable is ~20 nm for pyrites with total Au content of 2 ppm or less. The size of detectable Au nanoinclusions increases to 100 nm for pyrites with 100 ppm Au. Thus, if more than one nanoparticle is intercepted simultaneously they will register as a single particle in the depth profile.

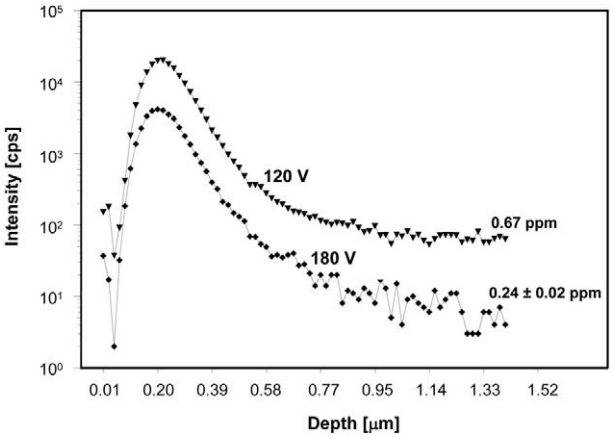

Fig. 2. Depth profiles conducted on Au-implanted Elba pyrite containing 5 ppb Au and 900 ppm As. The Au implant dosage and energy were 5×10^{13} Au atoms and 1 MeV, respectively. The quasigaussian curve corresponds to the implanted Au, and the flat portion represents the original Au plus isobaric molecular interference at 197 Daltons from CsS_2^+ and $FeAsS_2^+$. The depth profiles shown here illustrate how increasing voltage offset from 120 to 180 V decreased the molecular interference from 0.67 to 0.24 equivalent ppm Au. The concentration at the implant peak is ~200 ppm Au. For more details on how implants standards are used, the reader is referred to Chryssoulis (1989) and Cabri and McMahon (1995).

None of the techniques listed above can image the structure of arsenian pyrite overgrowths below the micrometer level, nor resolve individual Au nanoparticles. To investigate the nanometer-scale structure of selected arsenian pyrite overgrowths, HRTEM observation was performed at the University of Michigan Electron Microbeam Analysis Laboratory.

TEM samples were ultrasonically cut from thin sections, SJ-323C-1326 (Screamer) and DS-03-04 (Deep Star), mounted on 3-mm-diameter Cu grids, and polished. Using a tripod polishing method, a thin edge that intersected the thin As-rich overgrowths was created. HRTEM sample preparation was restricted to arsenian pyrite grains with anomalously thick arsenian pyrite overgrowths (>20 μm). Final thinning was carried out by milling with an Ar ion beam (4.0 keV) in a Gatan precise ion-polishing system (<30 min./sample). To minimize contamination, the TEM specimen holder was cleaned by plasma (Fischione model C1020). Observation was carried out using a JEOL JEM2010F field-emission high-resolution transmission electron microscope, with an EDAX energy dispersive x-ray spectrometer (EDS, ~1 wt.% detection limit). Nanometer-scale atomic mass contrast images were obtained using high-angle annular dark field scanning transmission electron microscopy (HAADF-STEM), discussed in detail by Utsunomiya and Ewing (2003). In these images, Au-rich zones appear brighter than iron sulfide matrix of lower average atomic mass Z (Palenik et al., 2004). The instrument used in this study has the following specifications: Cs = 1.0 nm, probe sizes are 0.2 nm for high-resolution HAADF-STEM and 0.5 nm for the analyses, the collection angle of the HAADF detector is 50–110 mrad, the condenser aperture size is 20 μm, and the defocus condition is ~−55 nm. Alteration of arsenian pyrite due to beam damage was tested and not observed during examination, as described by Palenik et al. (2004).

Gatan Digital Micrograph 3.4 software was used for image processing, including fast Fourier transformation (FFT).

4. ANALYTICAL RESULTS

4.1. Maximum Au and As Contents: EMPA and SIMS Data

Representative EMPA Au and As measurements of arsenian pyrite overgrowths in samples from Screamer, Meikle, Deep Star, and Porgera are summarized in Table 1. The narrow arsenian pyrite rims (<5–10 μm) polish poorly and are susceptible to beam damage. As a result, analyses often show low totals (<95 wt.%). From 250 spots analyzed, only 78 analyses have >97 wt.% total, considered the best and most representative results. Au contents range from maximum values of 9250 ppm (sample 48-1) to minimum values of 270 ppm (sample DS-03-04), and As ranges from a maximum of 19.76 wt.% (DS-03-04) to a minimum of 1.09 wt.% (P-62). Other trace elements, such as Ni, Se, Te, and Hg were measured only in some samples (Table 1). Ni and Hg were detected only in Deep Star samples (0.04–1.37 wt.%, and 0.35–1–38 wt.%, respectively), and traces of Se and Te were detected in samples from Meikle, Deep Star, and Porgera. Apart from Au and As, the only other trace element that was measured systematically is Sb, with contents varying from ~0.08 wt.% up to ~5 wt.%. The EMPA results show an antithetic correlation of As with S in arsenian pyrite (Fig. 3a), as previously documented by Fleet and Mumin (1997), consistent with the substitution of As for S in the pyrite structure (Fig. 3a). In contrast, Fe and Au contents in Figure 3b show a scattered pattern, with no clear correlation between the two elements. No correlation is observed between Sb and S, As, Au, or Fe.

Table 2 summarizes maximum, minimum, and average contents of 412 Au-As SIMS analyses of Au-bearing arsenian pyrite grains from the Lower Post, Mule Canyon, and Kirazli deposits. Individual Au-As analyses are presented in the Appendix. Because of its lower detection limits, the SIMS method yields analyses that cover a much wider range of Au and As concentrations than the EMPA analyses. Concentrations of Au range from a maximum of 2392 ppm to a minimum of 0.15 ppm, and As ranges between a maximum of 13.43 wt.% and a minimum of 0.003 wt.%. When the new SIMS and EMPA data from Carlin-type deposits are plotted along with the previously published data summarized in Figure 1 almost all data points fall within a well defined wedge-shaped region, limited above by a sharp boundary (Fig. 4). Most EMPA analyses of individual arsenian pyrite grains that fall in this region (e.g., DS-03-04) display a generally positive correlative between Au and As, whereas samples plotting above the upper boundary (e.g., SJ-323C-1326, abbreviated SJ-1326) show a wide range of Au contents at essentially a single As content, resulting in a vertical pattern (Fig. 4, inset).

SIMS and EMPA analyses of arsenian pyrite from epithermal Au deposits at Mule Canyon and Kirazli, when plotted along with previously published data from Emperor (Pals et al., 2003) define a similar wedge-shaped region in Au-As space (Fig. 5). Anomalous data points from Kirazli plot above this upper limit, and SIMS depth-profiling of this sample (Turk-21) reveals the presence of submicron inclusions (nanoparticles) of Au (Fig. 6). Figure 6 shows depth-concentration profiles (time vs. intensity in counts per second) of ^{34}S, ^{56}Fe, ^{75}As, and ^{197}Au for SIMS analyses of Turk-21. While the distribution of Fe, S, and As is constant with depth, the three well defined Au spikes suggest the presence of nanoparticulate Au (1–10 nm) in these arsenian pyrites. Pals et al. (2003) detected Au-Te inclusions in an arsenian pyrite sample from Emperor on SIMS depth profiles, and that sample (39PY53) also plots above the upper limit for Au in Figure 5.

4.2. HRTEM Constraints on the Form of Au

SIMS and EMPA data presented in the previous section indicate the presence of nanoparticulate Au in arsenian pyrite samples that plot above the upper limit of the wedge-shaped zones shown in Figures 4 and 5, consistent with XANES-EXAFS data by Simon et al. (1999a) (Fig. 1). To test this hypothesis and obtain further insight into the mineralogic setting of Au at the nanoscale, HRTEM observations were completed on samples SJ-323C-1326 (Screamer) and DS-03-04 (Deep Star), which plot above and below the Au-As limit (Fig. 4, inset), respectively. Figure 7a shows a representative HAADF image of the As-rich pyrite overgrowth in sample SJ-323C-1326 from Screamer, which exhibits the vertical relation between Au and As noted above for Figure 4 (inset). Discrete, submicron-sized particles of native Au in the As-rich pyrite overgrowths are observed, consistent with HRTEM observations of this sample made by Palenik et al. (2004). The bright, high average atomic mass (Z) particles are disseminated throughout a lower-Z arsenian pyrite matrix, with an estimated abundance of ~4% by volume. The Au particles range in size between ~5 and ~10 nm, and they were identified as native Au by EDS and fast Fourier transformation (FFT) of HRTEM images. A high magnification (4×10^6 times) HAADF image of an individual Au nanoparticle (labeled "S") shows its rounded shape and well defined boundaries as well as the array of Au atoms (Fig. 7b). In addition to the significant amount of Au shown by HRTEM observations to be present as nanoparticles of Au^0, a considerable amount of Au may be present also as structurally bound Au^{+1} at concentrations below the minimum detection limit of the EDS (~1 wt.%). A detailed HRTEM characterization of Au nanoparticle–bearing arsenian pyrite matrix was performed by Palenik et al. (2004). They found that the matrix surrounding the Au nanoparticles appears to be a polycrystalline mixture of randomly oriented pyrite and arsenopyrite (or pyrrhotite) domains (~20 nm^2). Our arsenian pyrite matrix HRTEM observations of this sample are consistent with their previous results.

Figure 8a shows a HAADF image of an arsenian pyrite rim from sample DS-03-04 (Deep Star). EMPA measurements of arsenian pyrite overgrowths from this sample reveal a positive correlation between Au and As (Fig. 4, inset). A representative HAADF image shows that Au nanoparticles are absent throughout the As-rich rim. Although solid-solution Au was not detected by EDS, which has a detection limit of about <1 wt.%, EMPA analyses detected up to 2960 ppm (0.2960 wt.%) Au. The lack of nanoparticulate Au suggests that solid solution accounts for all of the Au in this sample. HAADF images of arsenian pyrite (Fig. 8a) show As-enriched layers, which can be observed as brighter Z contrast. Although differences in Z contrast were observed on HAADF images throughout the sample, a representative HRTEM image shows a homogeneous and crystalline As-rich matrix (Fig. 8b). Selected area electron diffraction pattern (SAED) of this area (Fig. 8b, inset) reveal a

Table 1. Representative EMPA Au-As analyses (wt.%) of arsenian pyrite from Screamer, Deep Star, Meikle, and Porgera deposits. Detection limits are presented below each element label. b.d. = below detection; n.d. = not detected.

Sample	Fe (0.03)	S (0.05)	As (0.02)	Ni (0.03)	Co (0.02)	Se (0.01)	Te (0.03)	Sb (0.03)	Au (0.03)	Hg (0.05)	Total
Screamer											
SJ-323C-1138	41.64	45.78	9.71	b.d.	b.d.	b.d.	b.d.	3.51	0.12	b.d.	100.76
	43.24	46.78	8.45	b.d.	b.d.	b.d.	b.d.	2.90	0.10	b.d.	101.47
	42.89	46.63	8.37	b.d.	b.d.	b.d.	b.d.	3.38	0.09	b.d.	101.36
	43.28	47.72	6.76	b.d.	b.d.	b.d.	b.d.	3.85	0.12	b.d.	101.73
	43.67	48.42	6.12	b.d.	b.d.	b.d.	b.d.	2.74	0.16	b.d.	101.11
	43.56	48.01	6.23	b.d.	b.d.	b.d.	b.d.	3.63	0.13	b.d.	101.56
	43.94	48.35	6.15	b.d.	b.d.	b.d.	b.d.	2.49	0.18	b.d.	101.11
	45.15	50.21	4.17	b.d.	b.d.	b.d.	b.d.	1.16	0.08	b.d.	100.77
SJ-323C-1326(*)	42.56	48.56	6.93	b.d.	b.d.	b.d.	b.d.	1.18	0.59	b.d.	99.82
	39.89	46.56	8.46	b.d.	b.d.	b.d.	b.d.	2.19	0.70	b.d.	97.81
	42.09	47.36	8.07	b.d.	b.d.	b.d.	b.d.	0.71	0.84	b.d.	99.06
	40.72	47.09	7.77	b.d.	b.d.	b.d.	b.d.	1.96	0.56	b.d.	98.11
	41.13	45.67	8.53	b.d.	b.d.	b.d.	b.d.	1.28	0.71	b.d.	97.32
	42.13	46.99	7.90	b.d.	b.d.	b.d.	b.d.	0.83	0.76	b.d.	98.60
	40.83	46.04	7.94	b.d.	b.d.	b.d.	b.d.	2.24	0.63	b.d.	97.69
	41.13	45.48	8.25	b.d.	b.d.	b.d.	b.d.	1.54	0.64	b.d.	97.04
	41.22	46.29	7.31	b.d.	b.d.	b.d.	b.d.	2.11	0.37	b.d.	97.29
	39.82	46.06	7.93	b.d.	b.d.	b.d.	b.d.	2.58	0.70	b.d.	97.09
SJ-323C-902	42.77	47.24	8.11	b.d.	b.d.	b.d.	b.d.	2.88	0.30	b.d.	101.30
SJ-323C-987	43.64	51.64	4.33	b.d.	b.d.	b.d.	b.d.	1.53	0.05	b.d.	101.18
	44.08	52.51	3.30	b.d.	b.d.	b.d.	b.d.	1.33	0.07	b.d.	101.29
	43.64	52.10	1.40	b.d.	b.d.	b.d.	b.d.	1.62	0.09	b.d.	98.84
	40.02	47.80	4.70	b.d.	b.d.	b.d.	b.d.	4.44	0.22	b.d.	97.18
	42.32	48.94	6.22	b.d.	b.d.	b.d.	b.d.	2.89	0.19	b.d.	100.56
	42.65	49.68	4.44	b.d.	b.d.	b.d.	b.d.	4.15	0.13	b.d.	101.04
	41.45	47.90	5.75	b.d.	b.d.	b.d.	b.d.	5.36	0.24	b.d.	100.69
	42.32	49.53	4.08	b.d.	b.d.	b.d.	b.d.	4.37	0.14	b.d.	100.44
	43.64	51.60	1.65	b.d.	b.d.	b.d.	b.d.	2.54	0.11	b.d.	99.52
	41.74	49.67	5.06	b.d.	b.d.	b.d.	b.d.	4.38	0.11	b.d.	100.96
Deep Star											
DS-03-04	43.22	47.73	8.54	0.13	n.d.	0.05	n.d.	0.24	0.08	0.49	100.48
	39.36	39.69	19.76	0.04	n.d.	0.10	b.d.	b.d.	0.23	1.11	100.29
	39.53	41.21	17.68	b.d.	n.d.	0.09	b.d.	b.d.	0.29	1.27	100.08
	39.34	41.16	17.23	b.d.	n.d.	0.08	b.d.	b.d.	0.30	1.38	99.48
	39.16	40.35	19.11	b.d.	n.d.	0.10	b.d.	b.d.	0.29	1.25	100.25
	45.00	50.73	3.81	0.09	n.d.	0.04	n.d.	0.37	0.03	0.17	100.23
	40.31	41.70	17.26	b.d.	n.d.	0.09	n.d.	b.d.	0.22	1.23	100.81
	43.35	48.23	7.97	b.d.	n.d.	0.06	n.d.	0.66	0.06	0.40	100.73
	41.84	45.95	10.86	b.d.	n.d.	0.06	b.d.	0.40	0.10	0.67	99.88
	41.58	45.43	11.85	0.18	n.d.	0.07	n.d.	0.31	0.13	0.77	100.31
	41.71	47.51	8.45	1.37	n.d.	0.05	n.d.	0.24	0.03	0.35	99.71
	40.55	45.06	11.64	0.96	n.d.	0.07	n.d.	0.14	0.09	0.46	98.98
	40.79	44.39	10.50	0.14	n.d.	0.06	b.d.	0.20	0.13	0.52	96.73
	39.67	42.73	15.01	0.40	n.d.	0.07	b.d.	0.08	0.15	0.70	98.81
	40.79	46.07	11.28	0.18	n.d.	0.07	n.d.	b.d.	0.09	0.56	99.04
	39.99	45.01	12.22	0.04	n.d.	0.05	n.d.	b.d.	0.22	0.58	98.11
	42.79	48.43	7.72	0.22	n.d.	0.06	n.d.	0.23	0.05	0.39	99.88
	41.22	48.29	7.68	0.25	n.d.	0.06	n.d.	0.24	0.07	0.51	98.31
	41.21	46.81	9.44	b.d.	n.d.	0.06	n.d.	0.15	0.08	0.54	98.29
	41.44	45.19	12.81	0.04	n.d.	0.07	b.d.	0.08	0.12	0.51	100.25
	40.11	44.18	13.11	0.03	n.d.	0.06	n.d.	0.13	0.14	0.53	98.27
	40.24	43.48	15.45	0.22	n.d.	0.07	b.d.	b.d.	0.19	1.22	100.86
	44.85	51.60	4.07	b.d.	n.d.	0.05	n.d.	n.d.	0.07	0.42	101.07
Meikle											
M-2B	44.50	51.80	2.80	n.d.	n.d.	n.d.	n.d.	1.14	0.10	n.d.	100.34
	44.92	51.19	2.63	n.d.	n.d.	n.d.	n.d.	0.94	0.06	n.d.	99.73
	45.39	51.62	2.19	n.d.	n.d.	n.d.	n.d.	1.31	0.07	n.d.	100.57
M-03-08	44.32	50.50	2.86	b.d.	n.d.	b.d.	n.d.	0.04	0.04	n.d.	97.75
	44.85	51.47	4.26	b.d.	n.d.	b.d.	n.d.	0.37	0.13	b.d.	101.08
	43.70	49.28	4.39	n.d.	n.d.	0.01	b.d.	0.35	0.14	b.d.	97.87
	42.40	45.25	9.44	b.d.	n.d.	0.03	n.d.	b.d.	0.06	n.d.	97.18
M-03-08S	45.24	51.38	2.42	b.d.	n.d.	b.d.	b.d.	0.04	0.06	b.d.	99.13
M-03-12	44.85	49.42	2.57	b.d.	n.d.	b.d.	b.d.	b.d.	0.03	n.d.	96.87
M-03-10	42.54	49.82	3.62	b.d.	n.d.	b.d.	b.d.	0.04	0.04	b.d.	96.06
	40.89	47.92	9.43	b.d.	n.d.	0.02	n.d.	0.05	0.08	b.d.	98.39
Porgera											
P-62	43.47	49.72	3.84	b.d.	n.d.	b.d.	0.11	b.d.	0.16	n.d.	97.31
	44.45	50.67	3.06	b.d.	n.d.	b.d.	0.04	b.d.	0.19	n.d.	98.43

Table 1. (Continued)

Sample	Fe (0.03)	S (0.05)	As (0.02)	Ni (0.03)	Co (0.02)	Se (0.01)	Te (0.03)	Sb (0.03)	Au (0.03)	Hg (0.05)	Total
P-62 (cont.)	44.34	51.37	2.15	b.d.	n.d.	b.d.	0.07	b.d.	0.08	b.d.	98.05
	44.35	50.97	2.37	b.d.	n.d.	b.d.	0.16	b.d.	0.32	b.d.	98.21
	43.14	50.78	1.91	b.d.	n.d.	b.d.	0.75	b.d.	0.67	b.d.	97.29
	43.68	49.69	3.82	b.d.	n.d.	b.d.	0.16	b.d.	0.14	b.d.	97.53
	44.50	50.96	2.47	b.d.	n.d.	b.d.	0.07	b.d.	0.12	b.d.	98.15
	43.53	51.28	2.83	b.d.	n.d.	b.d.	0.11	n.d.	0.22	b.d.	98.01
	43.67	50.17	3.60	b.d.	n.d.	b.d.	0.16	b.d.	0.53	b.d.	98.17
	44.83	51.86	1.09	b.d.	n.d.	b.d.	0.09	b.d.	0.04	n.d.	97.94
	43.83	50.25	3.68	b.d.	n.d.	b.d.	0.15	b.d.	0.18	b.d.	98.13
	44.78	50.71	3.29	b.d.	n.d.	b.d.	0.06	b.d.	0.06	b.d.	98.92
	44.70	51.36	2.27	b.d.	n.d.	b.d.	0.16	n.d.	0.35	n.d.	98.84
48-1	44.27	48.69	3.38	b.d.	n.d.	b.d.	b.d.	b.d.	0.93	b.d.	97.35
	44.47	49.09	2.80	b.d.	n.d.	b.d.	b.d.	b.d.	0.91	b.d.	97.35

(*) Au-As for this sample previously reported by Palenik et al. (2004).

distortion from the pure pyrite structure (FeS_2, *Pa3*) lattice parameters. Such a deviation may be consistent with the high As content that is contained in the rims (up to ~10 wt.% As), although an arsenopyrite-like structure cannot be ruled out. Considering an arsenopyrite structure (FeAsS, *P21/c*), indexing of the SAED pattern in Figure 7b shows a smaller deviation from the arsenopyrite unit cell parameters. Fleet at al. (1989) and Simon et al. (1999a) observed 10-Å stacking faults in arsenian pyrite, suggesting arsenopyrite or marcasite interlayering. Although this feature was not observed in our HRTEM images, the presence of two or more As-bearing iron sulfide phases cannot be ruled out as possible hosts for solid-solution Au.

5. DISCUSSION

5.1. Solubility Limit of Au in Arsenian Pyrite

SIMS and EMPA analyses presented in this study confirm that the amount of Au that can be accommodated by arsenian pyrite is directly related to its As content. When new and previously published data are plotted together in summary Figure 9, the sharp upper limit for Au divides the log (Au)–log (As) space into two different fields: (a) a well defined wedge-shaped lower field configured by most of the data points, and (b) an upper field above the latter one, containing anomalous data points of high Au/As molar ratios. Based on the analytical evidence presented in the previous sections, we propose that the upper limit of the wedge-shaped zone in Figure 9 represents a limit for solid solution of Au in arsenian pyrite. This limit can be approximated by a line of the form

$$C_{Au} = 0.02 \cdot C_{As} + 4 \times 10^{-5} \quad (1)$$

in which C_{Au} and C_{As} represent the concentrations of Au and As in mole percent (mol%). The slope of this line is defined by a limiting Au/As molar ratio of 0.02, where one Au atom is related to 50 As atoms. HRTEM observations and SIMS measurements of selected samples in both of these fields revealed that in samples located below the limit, the dominant form of Au is solid solution (Au^{+1}), whereas samples plotting above

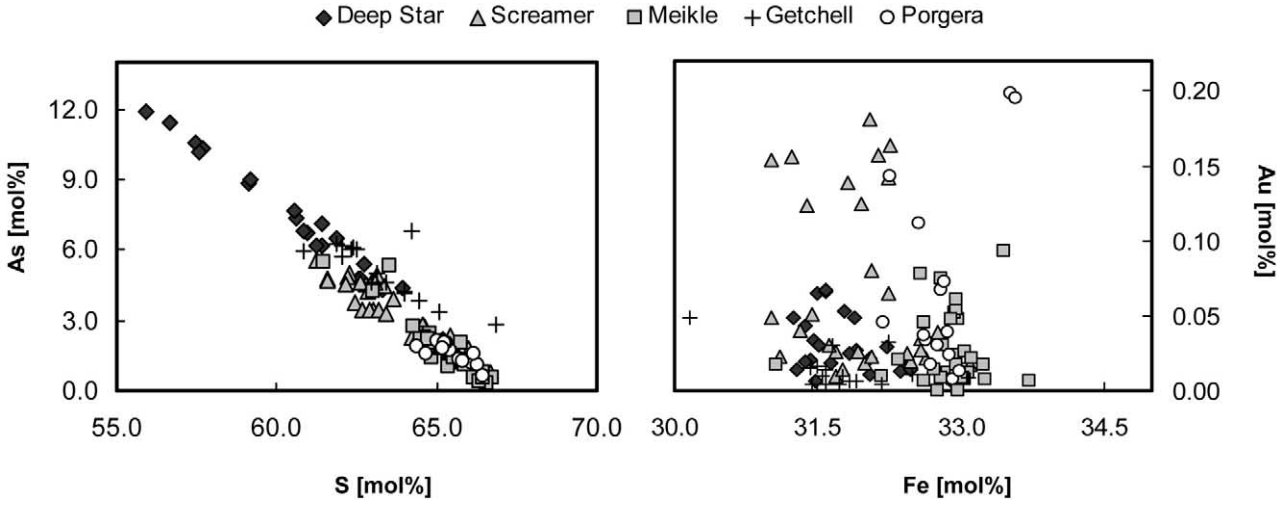

Fig. 3. Distribution of (a) As vs. S and (b) Fe vs. Au for EMPA analyses from Carlin-type and epithermal deposits. Additional data from Getchell and Meikle taken from Cline (2001) and Emsbo et al. (2003), respectively.

Table 2. Summary statistics of SIMS Au-As analyses (Appendix) of arsenian pyrite from Lower Post (Nevada), Mule Canyon (Nevada), and Kirazli (Turkey). Mean concentrations (<X>) are reported along with standard errors (σ).

Deposit	Datapoints		As (wt.%)	Au (ppm)
Lower Post	290	max.	13.43	2392.00
		min.	0.01	0.15
		<X> ± σ	1.72 ± 0.13	117.48 ± 15.18
Mule Canyon	73	max.	5.50	1691.10
		min.	0.01	0.40
		<X> ± σ	1.02 ± 0.17	64.13 ± 24.27
Kirazli	49	max.	0.70	115.00
		min.	0.003	0.30
		<X> ± σ	0.16 ± 0.03	21.67 ± 4.03

this limit contain significant amounts of Au in the form of native Au nanoparticles (Au^0). These analytical observations confirm the prediction based on XANES-EXAFS data included in Figure 1. According to Eqn. 1, the solubility of Au in As-free pyrite ($C_{As} = 0$) is predicted to be ~1.5 ppm (4×10^{-5} mol%), in good agreement with the experimental solubility of Au in pure pyrite, 3 ± 1 ppm, as determined by Tauson (1998, 1999). Furthermore, linear extrapolation of the upper limit (Eqn. 1 to the As content of stoichiometric arsenopyrite (~33 mol% or 46 wt.% As) predicts a maximum Au content of ~0.6 mol% (~2 wt.%), as can be seen in Figure 9. This value lies between the maximum amounts reported for natural (~1.5 wt.% Au; Johan et al., 1989) and synthetic arsenopyrites (~1.7 wt.% Au at 500°C and 2 kbar by Wu and Delbove, 1989; ~3 wt.% Au at 400°C and 1.5 kbar by Fleet and Mumin, 1997).

The substitution of S by As in the pyrite structure is sup-

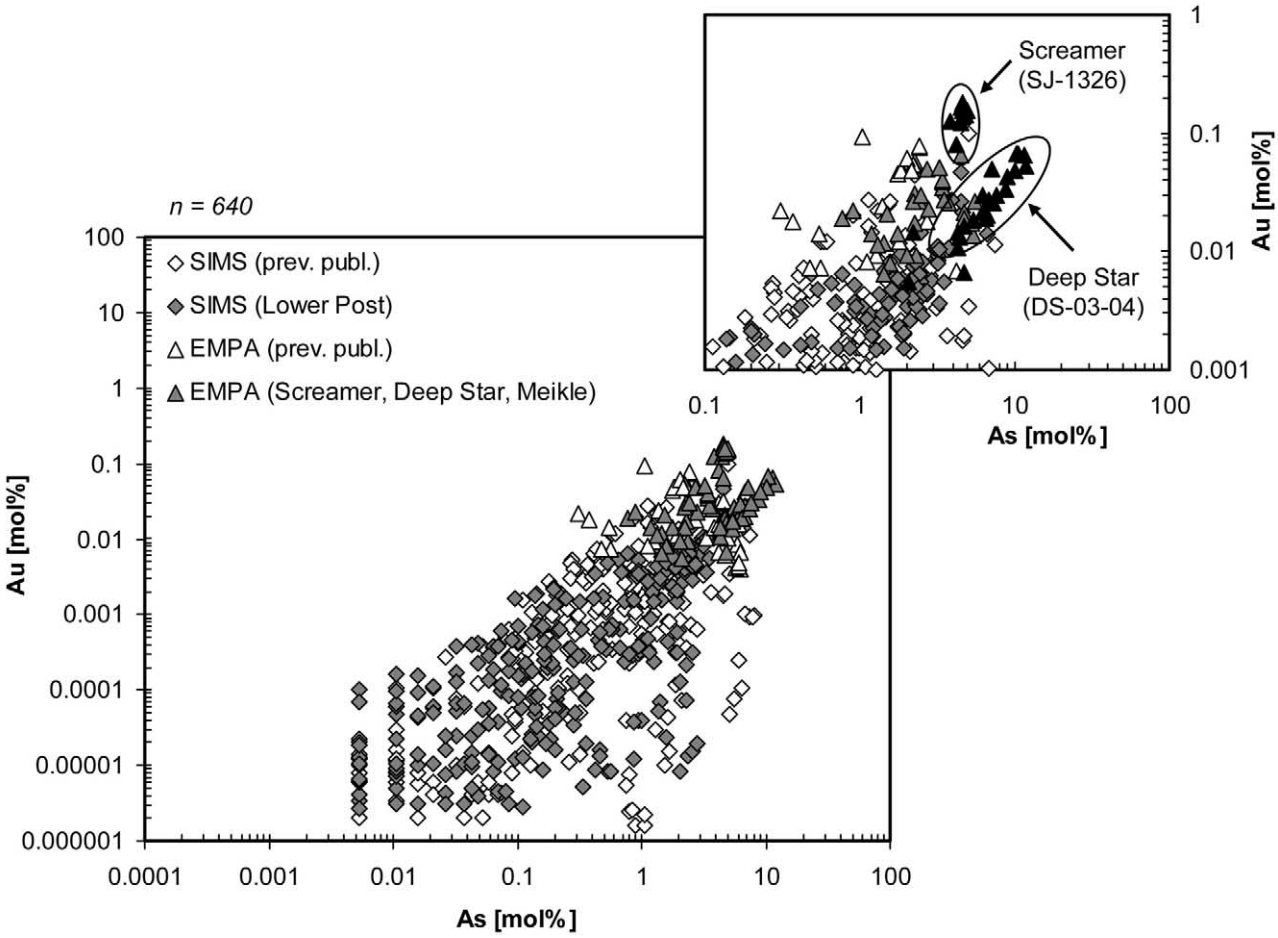

Fig. 4. Au-As plot of new SIMS and EMPA analyses from various Carlin-type deposits combined with those from Figure 1. Inset shows detailed structure of EMPA Au-As analyses of two representative samples from Screamer (SJ-323C-1326, abbreviated SJ-1326) and Deep Star (DS-03-04). Additional sources of data cited in caption for Figure 1.

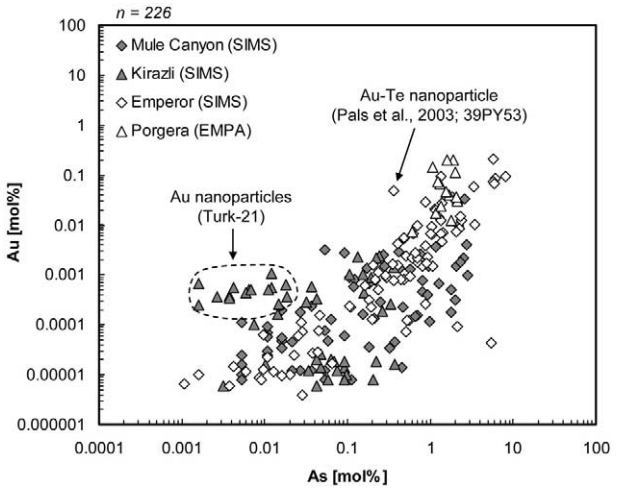

Fig. 5. Au-As plot of new SIMS and EMPA analyses of arsenian pyrite from epithermal Au deposits. A sample from Kirazli (Turk-21, circled) contains submicron inclusions (nanoparticles) of Au (see Fig. 6). Additional SIMS data from Emperor taken from Pals et al. (2003).

ported by EMPA data (Fig. 3a) and previous spectroscopic data (Simon et al., 1999a; Savage et al., 2000). In contrast, the substitutional mechanism(s) of Au incorporation into solid solution remain unclear. Solid-solution Au is incorporated in arsenopyrite replacing Fe as Au^{+1}, based on the observed anticorrelation between the two elements and micro-XANES spectroscopic data (Johan et al., 1989; Wu and Delbove, 1989; Tarnocai at el., 1997; Cabri et al., 2000). However, other studies have found no significant correlation, suggesting that Au is incorporated nonsystematically into lattice defects (vacancies) in arsenopyrite (Aylmore, 1995; Fleet and Mumin, 1997). Although the most appealing mechanism for Au incorporation into arsenian pyrite would be its substitution for Fe in the octahedral sites, Au-Fe EMPA data in Figure 3b do not show consistent linear trends to support this mechanism of incorporation. However, even though Au and Fe do not correlate systematically, Au substitution for Fe cannot be ruled out completely. XANES-EXAFS data from Simon et al. (1999a) suggest that solid-solution Au in arsenian pyrite is incorporated in two coordination environments, as twofold (as Au_2S compound) and fourfold. The latter could be found in one or more forms, including Au^{+1} in a vacancy position, as an unknown Au-As-S compound or in a distorted Fe^{+2} octahedral site. Thus, multiple mechanisms of Au incorporation (e.g., into vacancies, defects, and octahedral sites) into pyrite may account for the scattered patterns observed in Figure 3b. In addition, the observed Fe deficiency (Fe <~31–~33 mol%) does not correlate with other elements that are present in arsenian pyrite (e.g., Hg, Ni, Sb, Se, Te), hence structural vacancies may account for the nonstoichiometric Fe contents.

It has been suggested that the incorporation of solid-solution Au in arsenian pyrite would be nonsystematic in terms of crystal-chemical parameters, depending only on solution conditions imparting a minimum excess of As and a deficiency of Fe to the active growth surface (Fleet and Mumin, 1997). If adsorption of Au complexes (e.g., $Au(HS)^0_{(aq)}$ or $Au(HS)^-_{2\,(aq)}$) onto growing As-rich pyrite surfaces is a feasible mechanism under hydrothermal conditions (Sha, 1993; Fleet and Mumin, 1997; Widler and Seward, 2002), incorporation of Au into arsenian pyrite has to be strongly dependent on the availability of vacant sites and/or defects on the surface, as well as the presence of As. Although the actual effect of As in pyrite surfaces still remains unresolved, As coatings may facilitate the adsorption of Au complexes by causing *n*-type semiconducting properties of pyrite to become locally *p*-type, giving them a stronger electrochemical interaction with negatively charged ions (Prokhorov and Lu, 1971; Mironov et al., 1981; Maddox et al., 1998). The maximum solubility of Au into arsenian pyrite will thus be a function of the As content on the surface as well as of the availability of vacant sites and/or structural defects. Metastable arsenian pyrite found in Carlin-type and epithermal deposits may have formed rapidly under nonequilibrium conditions at low temperatures (T <250°C), giving it the ability to incorporate significant amounts of Au, As, and other trace metals in solid solution, favored by the availability of extra vacancies and surface defects resulting from rapid growth and disequilibrium.

5.3. Geologic Significance of the Solubility Limit

Available information suggests that the effect of temperature on the solubility limit shown in Figure 9 is relatively minor for low-temperature hydrothermal geologic environments. Carlin-type and epithermal deposits, which supplied all of the samples used in this study, form at temperatures between ~150°C and ~250°C (Hayba et al., 1985; Hosftra and Cline, 2000). The fact that the limit in Figure 9 is well defined suggests that the solubility limit does not vary greatly with temperature for this range of temperatures. However, arsenian pyrite is also found in much lower-temperature diagenetic environments as well as in greenstone and orogenic Au deposits that form at temperatures of up to 300°C, and our present data do not preclude the possibility of temperature-related variations in the solubility

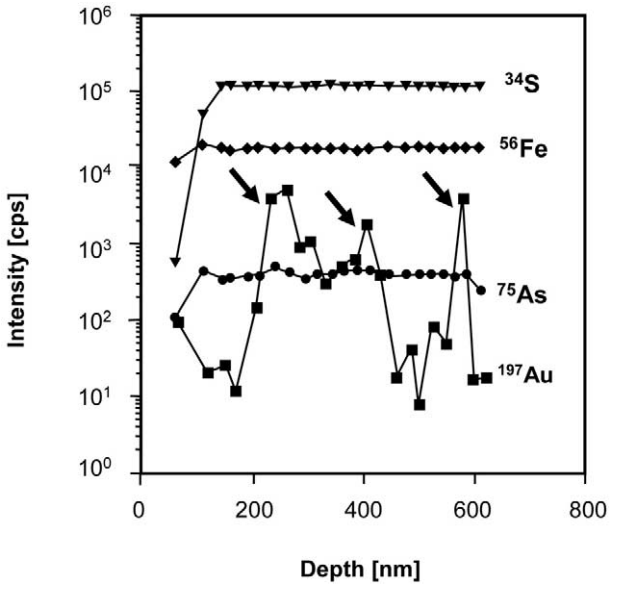

Fig. 6. SIMS depth-concentration profiles (time vs. intensity) of ^{197}Au, ^{75}As, ^{56}Fe, and ^{34}S for sample Turk-21 from Kirazli. Arrows indicate spikes suggesting the presence of submicrometer inclusions of Au.

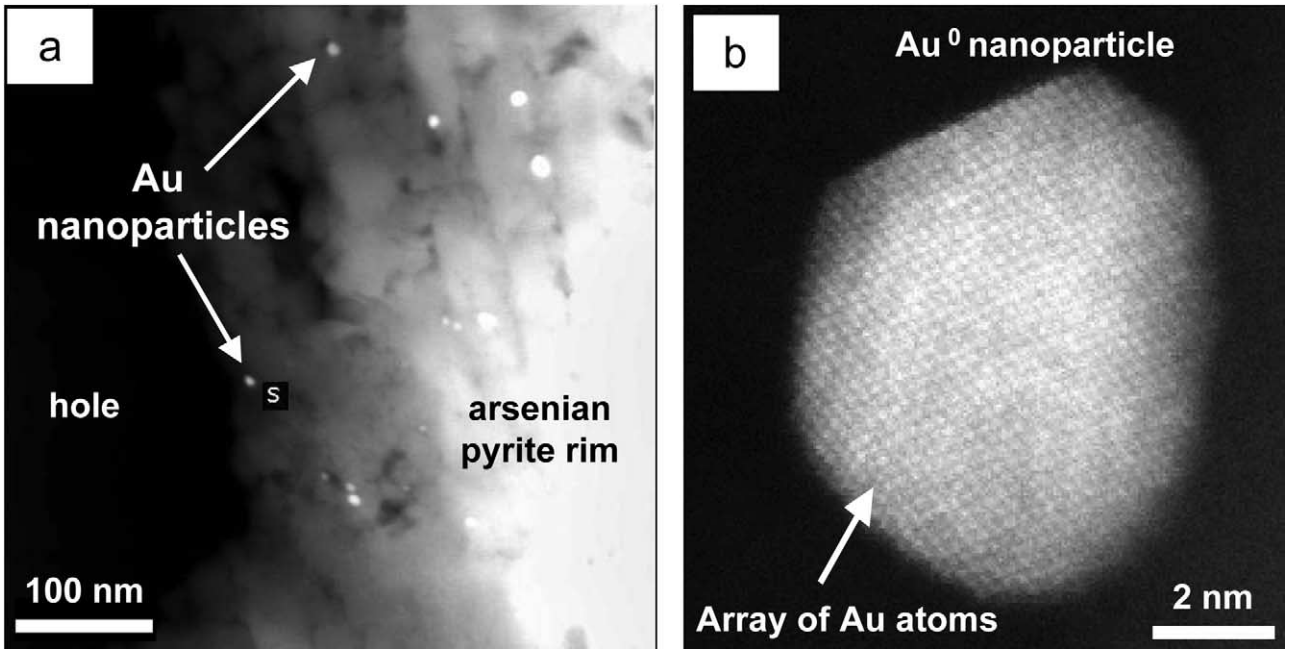

Fig. 7. High-angle annular dark field (HAADF) images of arsenian pyrite rims from sample SJ-323C-1326 (Screamer). (a) Bright, high average atomic mass (Z) contrast Au particles are disseminated throughout a lower-Z arsenian pyrite matrix. (b) High-magnification (4×10^6 times) image of an individual Au nanoparticle (labeled "S") shows the rounded shape and well defined boundaries of the particle, as well as the array of Au atoms.

limit for Au at these lower and higher temperatures. Within the 150°C–250°C range for which Figure 9 was compiled, Au-As relations can be used to predict the dominant chemical form of Au in arsenian pyrite. Furthermore, measured Au and As contents of arsenian pyrites relative to the upper limit of the wedge-shaped zone can be used as an indicator of the saturation state of Au in hydrothermal solutions from which they were deposited. In Carlin-type deposits, almost all of the Au-As

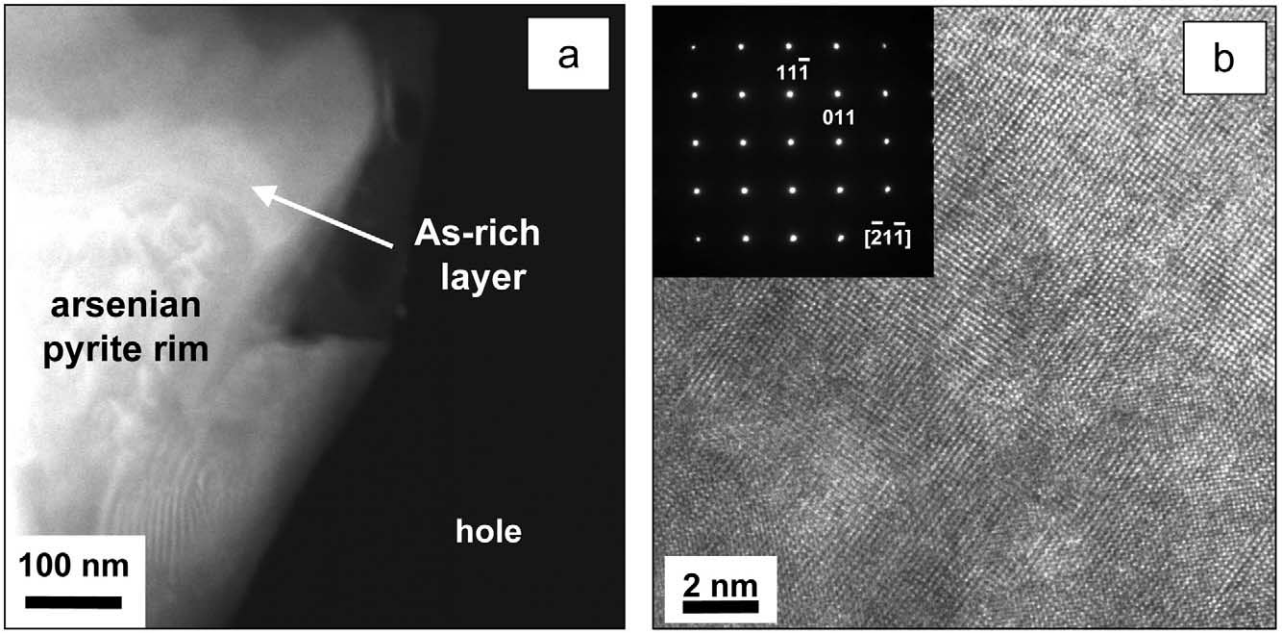

Fig. 8. High-angle annular dark field (HAADF) images of arsenian pyrite rims from sample DS-03-04 from Deep Star. (a) Arsenian pyrite rim shows As-enriched layers, which can be observed as brighter Z-contrast areas. Native Au nanoparticles are absent. (b) HRTEM image shows a homogeneous and crystalline As-rich matrix. Selected area electron diffraction pattern (SAED) of this area (inset) reveals a distortion from the pure pyrite structure.

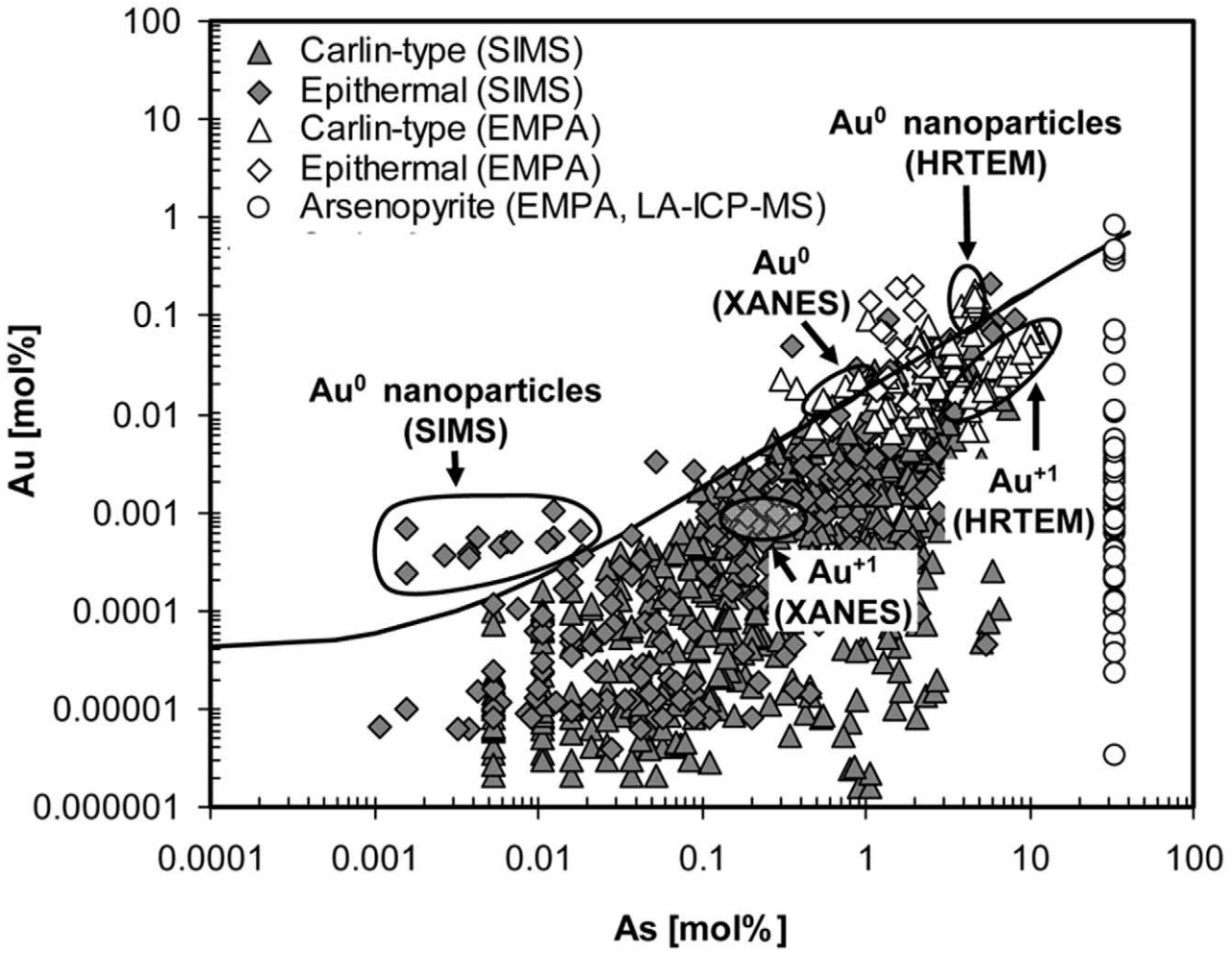

Fig. 9. Summary Au-As plot showing all SIMS and EMPA analyses of arsenian pyrite from Carlin-type and epithermal deposits. Analytical and spectroscopic data on the chemical state of Au in selected samples is included along with the compositional data. The inferred solubility limit for gold is approximated by the line $C_{Au} = 0.02 \cdot C_{As} + 4 \times 10^{-5}$, where C_{Au} and C_{As} represent the concentrations of Au and As in mole percent (mol%). Below this line, Au is present in solid solution (Au^{+1}), whereas above it a significant amount of Au is contained as nanoparticles of native Au (Au^0). Arsenopyrite data (circles) taken from Johan et al. (1989), Wu and Delbove (1989), Cook and Chryssoulis (1990), Fleet and Mumin (1997), and Hinchey et al. (2003).

analyses plot below the solubility limit in Figure 9, indicating that these arsenian pyrites formed from solutions that were not saturated with respect to Au^0 (Simon et al., 1999b). Depending on whether As was previously present in arsenian pyrite (reaction 1), or transported along with Au as an $HAsS_{2(aq)}$ complex (Spycher and Reed, 1989) (reaction 2), Au can be removed from solutions undersaturated with respect to native Au by adsorption reactions of $Au(HS)^0_{(aq)}$ complexes (Seward, 1973):

$$Fe(S, As)_2 + 2Au(HS)^0_{(aq)} = Fe(S, As)_2 \cdot Au_2S^0 + H_2S_{(aq)} \quad \text{(Reaction 1)}$$

$$Fe^{2+} + 2HAsS_{2(aq)} + 2Au(HS)^0_{(aq)} + 2H_{2(g)} = Fe(S, As)_2 \cdot Au_2S^0 + 3H_2S_{(aq)} + 2H^+ \quad \text{(Reaction 2)}$$

Reactions 1 and 2 are strongly dependent on the activity of $H_2S_{(aq)}$, and therefore a decrease in H_2S produced by either sulfidation (Carlin systems) or boiling (epithermal systems) strongly favors formation of arsenian pyrite and incorporation of Au as solid solution. This alternative mechanism may be responsible for the extraction and concentration of most of the "invisible" Au present in Carlin-type deposits. In epithermal systems, native (Au^0) and electrum (Au,Ag) are common, and arsenian pyrite compositions in Figures 4 and 5 plot well above the solubility limit. Along with the occurrence of colloidal-size Au and Au-Te inclusions detected by SIMS depth profiling (this study; Pals et al., 2003) and the presence of native Au, this confirms that the ore-forming solutions were saturated with respect to native Au.

Compositions of arsenian pyrite in Carlin-type and epithermal deposits indicate that the state of Au in their parent hydrothermal solutions differed significantly. Whereas solutions forming epithermal deposits were largely saturated with respect to Au, those that formed Carlin-type deposits were largely unsaturated and solid-solution Au was probably removed from fluids by adsorption

on metastable arsenian pyrite. The capacity of arsenian pyrite to concentrate Au from undersaturated solutions was apparently a key factor in the formation of giant Carlin-type deposits and could account for their unusually large size.

6. SUMMARY AND CONCLUSIONS

SIMS-EMPA analyses of Au-bearing arsenian pyrite from hydrothermal ore deposits show that Au-As compositions configure a wedge-shaped distribution in log (Au)–log (As) space. Maximum solid-solution Au contents are limited by an As-dependent upper limit, that can be approximated by a line of the form $C_{Au} = 0.02\ C_{As} + 4 \times 10^{-5}$ with a slope that defines a limiting Au/As molar ratio of 0.02. In samples located below the limit (Au/As $<$ 0.02), the dominant form of Au is solid solution (Au^{+1}), whereas anomalous samples plotting above this limit (Au/As $>$ 0.02) contain significant amounts of Au in the form of native Au nanoparticles (Au^0). Linear extrapolation of this limit downward to the composition of stoichiometric pyrite indicates Au contents of ~1.5 ppm, whereas extrapolation of the limit upward to the composition of stoichiometric arsenopyrite predicts the maximum Au content measured in natural and synthesized arsenopyrite (~2 wt.%).

These relations suggest that the upper limit of this wedge-shaped zone constitutes a solubility limit for solid solution of Au as a function of As for the temperature range between ~150°C and ~250°C. This solubility limit can be used to predict the dominant chemical form of Au in arsenian pyrite and the saturation state of Au in hydrothermal solutions that deposited the arsenian pyrite.

Acknowledgments—Support for this study was received from National Science Foundation grant EAR 0207273 to SEK, RCE, and Lumin Wang. Additional support was provided to MR by Rackham Graduate School at the University of Michigan through a fellowship and a Fulbright-Mecesup grant. We are grateful to Newmont Gold and Barrick Gold Corporations for logistical assistance and for releasing analytical data for publication, and specifically to Al Lander, Jerry Rahn, Pamela Zohar, and Steve Kulinsky at Barrick and Eric Saderholm and David Creel at Newmont for their help providing guidance during open-pit, underground, and core sampling related to this study. We also thank Jeremy Richards for providing samples from Porgera and Carl Henderson for invaluable help with EMPA analysis. The electron microprobe used in this work was acquired under from National Science Foundation grant EAR-99-11352. Finally, we acknowledge Richard L. Hervig, Frank K. Mazdab, Mark R. Frank, and an anonymous reviewer for helpful reviews of the manuscript. This research represents part of the first author's Ph.D. dissertation at the University of Michigan.

REFERENCES

Arehart G. B., Chryssoulis S. L., and Kesler S. E. (1993) Gold and arsenic in iron sulfides from sediment-hosted disseminated gold deposits; implications for depositional processes. *Econ. Geol.* **88,** 171–185.

Aylmore M. G. (1995) Distribution and agglomeration of gold in arsenopyrite and pyrite. Ph.D. thesis, Curtin Univ., Perth.

Bakken B. M., Hochella M. F. Jr., Marshall A. F., and Turner A. M. (1989) High-resolution microscopy of gold in unoxidized ore from the Carlin Mine, Nevada. *Econ. Geol.* **84,** 171–179.

Cabri L. J. and McMahon G. (1995) SIMS analysis of sulfide minerals for Pt and Au; methodology and relative sensitivity factors (RSF). *Can. Mineral.* **33,** 349–359.

Cabri L. J., Newville M., Gordon R. A., Crozier E. D., Sutton S. R., McMahon G., and Jiang D. (2000) Chemical speciation of gold in arsenopyrite. *Can. Mineral.* **38,** 1265–1281.

Chryssoulis S. L. (1989) Quantitative trace precious metal analysis of sulphide and sulpharsenide minerals by SIMS in secondary ion mass spectrometry. In *Proc. Int. Conf. SIMS VII* (eds. Benninghoven, Evans, McKeegan, Storms, and Werner). John Wiley & Sons, pp. 405–408.

Chryssoulis S. (1990) Detection and quantification of "invisible" gold by microprobe techniques. In *Proc. Symp. Gold 90′, Soc. for Mining, Metall. Explor.* (eds. Hausen D. M, Halbe D. N., Petersen, and E. U. Tafuri). W. J. Littleton, pp. 323–331.

Chryssoulis S. L., Cabri L. J., and Salter R. S. (1987) Direct determination of invisible gold in refractory sulphide ores. In *Proc. Internat. Symp. On Gold Metallurgy-Refract. Gold* (eds. R. S. Salter, D. M. Wyslouzil, and G. W. McDonald). Pergamon Press, pp. 235–244.

Chryssoulis S. L., Dunne R., and Coetzee A. (2004) Diagnostic microbeam technology in gold ore processing. *J. Min. Metall. Mater. Soc.* **56,** 53–57.

Clark L. A. (1960) The Fe-As-S system—Phase relations and applications. *Econ. Geol.* **55,** 1345–1381.

Cline J. S. (2001) Timing of gold and arsenic sulfide mineral deposition at the Getchell Carlin-type gold deposit, north-central Nevada. *Econ. Geol.* **96,** 75–89.

Cline J. S., Shields D., Riciputi L., Fayek M., Copp T., Muntean J., and Hosftra A. H. (2003) Trace element and isotope microanalyses support a deep ore fluid source at the Getchell Carlin-type gold deposit, northern Nevada. *Proc. Geol. Soc. Am. Abstr. Prog.* **35**, 358.

Cook N. J. and Chryssoulis S. L. (1990) Concentrations of invisible gold in the common sulfides. *Can. Mineral.* **28,** 1–16.

Emsbo P., Hofstra A. H., Lauha E. A., Griffin G. L., Hutchinson R. W., John D. A., and Theodore T. G. (2003) Origin of high-grade gold ore, source of ore fluid components and genesis of the Meikle and neighboring Carlin-type deposits, northern Carlin Trend, Nevada. *Econ. Geol.* **98,** 1069–1105.

Fleet M. E. and Mumin A. H. (1997) Gold-bearing arsenian pyrite and marcasite and arsenopyrite from Carlin Trend gold deposits and laboratory synthesis. *Am. Mineral.* **82,** 182–193.

Fleet M. E., MacLean P. J., and Barbier J. (1989) Oscillatory-zoned As-bearing pyrite from strata-bound and stratiform gold deposits; an indicator of ore fluid evolution. *Econ. Geol. Monog.* **6,** 356–362.

Fleet M. E., Chryssoulis S. L., MacLean P. J., Davidson R., and Weisener C. G. (1993) Arsenian pyrite from gold deposits; Au and As distribution investigated by SIMS and EMP and color staining and surface oxidation by XPS and LIMS. *Can. Mineral.* **31,** 1–17.

Friedl J., Wagner F. E., and Wang N. (1995) On the chemical state of combined gold in sulfidic ores: Conclusions from Mössbauer source experiments. *Neues Jahrbuch für Mineralogie-Abhandlungen* **169,** 279–290.

Hayba D. O., Bethke P. M., Heald P., and Foley N. K. (1985) Geologic, mineralogic and geochemical characteristics of volcanic-hosted epithermal precious-metal deposits. *Rev. Econ. Geol.* **2,** 129–167.

Heitt D. G., Dunbar W. W., Thompson T. B., Jackson R. G., Hofstra A. H., John D. A., and Theodore T. G. (2003) Geology and geochemistry of the Deep Star gold deposit, Carlin Trend, Nevada. *Econ. Geol.* **98,** 1107–1135.

Hinchey J. G., Wilton D. H. C., and Tubrett M. N. (2003) A LAM-ICP-MS study of the distribution of gold in arsenopyrite from the Lodestar prospect, Newfoundland, Canada. *Can. Mineral.* **41,** 353–364.

Hofstra A. H. and Cline J. S. (2000) Characteristics and models for carlin-type gold deposits. *Rev. in Econ. Geol.* **13,** 163–220.

Johan Z., Marcoux E., and Bonnemaison M. (1989) Arsenopyrite aurifere; mode de substitution de Au dans la structure de FeAsS. Auriferous arsenopyrite; substitution of Au in the Fe-As-S structure. *Comp. Rend. Acad. Sci., Serie 2* **308,** 185–191.

John D. A., Hofstra A. H., Fleck R. J., Brummer J. E., and Saderholm E. C. (2003) Geologic setting and genesis of the Mule Canyon low-sulfidation epithermal gold-silver deposit, north-central Nevada. *Econ. Geol.* **98,** 425–463.

Kolker A., Haack S. K., Cannon W. F., Westjohn D. B., Kim M. J., Nriagu J., and Woodruff L. G. (2003) Arsenic in southeastern Michigan. In *Arsenic in Ground Water* (eds. A. H. Welch and K. G. Stollenwerk). Kluwer Academic Publishers, Boston, pp. 281–294.

Kretschmar U. and Scott S. D. (1976) Phase relations involving arsenopyrite in the system Fe-As-S and their application. *Can. Mineral.* **14,** 364–386.

Leach B. R. (1993) Breccia characteristics of the Lower Post orebody, Eureka County, Nevada. *Geol. Soc. Nevada Sp. Publ.* **19,** unpag.

MacLean P. J. and Fleet M. E. (1989) Detrital pyrite in the Witwatersrand gold fields of South Africa; evidence from truncated growth banding. *Econ. Geol.* **84,** 2008–2011.

Maddox L. M., Bancroft G. M., Scaini M. J., and Lorimer J. W. (1998) Invisible gold; comparison of Au deposition on pyrite and arsenopyrite. *Am. Mineral.* **83,** 1240–1245.

Mironov A. G., Zhodik S. M., and Maksimova E. A. (1981) An experimental investigation of the sorption of gold by pyrites with different thermoelectric properties. *Geochem. Int.* **18,** 153–160.

Murowchick J. B. and Barnes H. L. (1986) Marcasite precipitation from hydrothermal solutions. *Geochim. Cosmochim. Acta* **50,** 2615–2629.

Palenik C. S., Utsunomiya S., Reich M., Kesler S. E., and Ewing R. C. (2004) "Invisible" gold revealed: direct imaging of gold nanoparticles in a Carlin-type deposit. *Am. Mineral.* **89,** 1359–1366.

Pals D. W., Spry P. G., and Chryssoulis S. L. (2003) Invisible gold and tellurium in arsenic-rich pyrite from the Emperor gold deposit, Fiji; implications for gold distribution and deposition. *Econ. Geol.* **98,** 479–493.

Pokrovski G. S., Kara S., and Roux J. (2002) Stability and solubility of arsenopyrite, FeAsS, in crustal fluids. *Geochim. et Cosmochim. Acta* **66,** 2361–2378.

Prokhorov V. G. and Lu L. V. (1971) Electrochemical and thermoelectric properties of pyrite as a criterion of the conditions of mineral formation. In *Mineralogiya i mineralogicheskaya kristallografiya (Mineralogy and Mineral Crystallography)*. Sverdlovsk, p. 115.

Radtke A. S. (1985) Geology of the Carlin gold deposit, Nevada. *Geol. Surv. Prof. Paper 1267*, 124 pp.

Radtke A. S., Heropoulos C., Fabbi B. P., Scheiner B. J., and Essington M. (1972) Data on major and minor elements in host rocks and ores, Carlin Gold Deposit, Nevada. *Econ. Geol.* **67,** 975–978.

Reich M., Palenik C. S., Utsunomiya S., Becker U., Stixrude L., Kesler S. E., and Ewing R. C. (2003) Solubility limit of gold in arsenian pyrite from Carlin-type and epithermal deposits: EMPA, SIMS, HRTEM and quantum mechanical constraints. *Proc. Geol. Soc. Am. Abstr. Prog.* **35**, 358.

Richards J. P. and Kerrich R. (1993) The Porgera gold mine, Papua New Guinea; magmatic hydrothermal to epithermal evolution of an alkalic-type precious metal deposit. *Econ. Geol.* **88,** 1017–1052.

Savage K. S., Tingle T. N., O'Day P. A., Waychunas G. A., and Bird D. K. (2000) Arsenic speciation in pyrite and secondary weathering phases, Mother Lode gold district, Tuolumne County, California. *Appl. Geochem.* **15,** 1219–1244.

Schoonen M. A. A. and Barnes H. L. (1991a) Reactions forming pyrite and marcasite from solution; I, Nucleation of FeS_2 below 100 degrees C. *Geochim. Cosmochim. Acta* **55,** 1495–1504.

Schoonen M. A. A. and Barnes H. L. (1991b) Reactions forming pyrite and marcasite from solution; II, Via FeS precursors below 100 degrees C. *Geochim. Cosmochim. Acta* **55,** 1505–1514.

Schoonen M. A. A. and Barnes H. L. (1991c) Mechanisms of pyrite and marcasite formation from solution; III, Hydrothermal processes. *Geochim. Cosmochim. Acta* **55,** 3491–3504.

Seward T. M. (1973) Thio complexes of gold and the transport of gold in hydrothermal ore solutions. *Geochim. et Cosmochim. Acta* **37,** 379–399.

Sha P. (1993) Geochemistry and genesis of sediment-hosted disseminated gold mineralization at the Gold Quarry mine, Nevada. Ph.D. thesis, Univ. of Alabama, Tuscaloosa.

Sidle W. C., Wotten B., and Murphy E. (2001) Provenance of geogenic arsenic in the Goose River basin, Maine, USA. *Environ. Geol.* **41,** 62–73.

Simon G. (1998) Geochemistry of gold and selenium in hydrothermal ore deposits. Ph.D. thesis, Univ. of Michigan, Ann Arbor.

Simon G., Huang H., Penner-Hahn J. E., Kesler S. E., and Kao L. S. (1999a) Oxidation state of gold and arsenic in gold-bearing arsenian pyrite. *Am. Mineral.* **84,** 1071–1079.

Simon G., Kesler S. E., and Chryssoulis S. L. (1999b) Geochemistry and textures of gold-bearing arsenian pyrite, Twin Creeks, Nevada; implications for deposition of gold in Carlin-type deposits. *Econ. Geol.* **94,** 405–421.

Spycher N. F. and Reed M. H. (1989) As(III) and Sb(III) sulfide complexes; an evaluation of stoichiometry and stability from existing experimental data. *Geochim. Cosmochim. Acta* **53,** 2185–2194.

Tarnocai C. A., Hattori K., and Cabri L. J. (1997) "Invisible" gold in sulfides from the Campbell mine, Red Lake greenstone belt, Ontario: Evidence for mineralization during the peak of metamorphism. *Can. Mineral.* **35,** 805–815.

Tauson V. L. (1998) On limit concentration and manner of incorporation of gold in hydrothermal pyrite. *Russ. Geol. Geophys.* **39,** 932–940.

Tauson V. L. (1999) Gold solubility in the common gold-bearing minerals; experimental evaluation and application to pyrite. *Eur. J. Mineral.* **11,** 937–947.

Tauson V. L., Pastushkova T. M., and Bessarabova O. I. (1998) On limit concentration and manner of incorporation of gold in hydrothermal pyrite. *Russ. Geol. Geophys.* **39,** 932–940.

Utsunomiya S. and Ewing R. C. (2003) Application of high-angle annular dark field scanning transmission electron microscopy, scanning transmission electron microscopy-energy dispersive x-ray spectrometry and energy-filtered transmission electron microscopy to the characterization of nanoparticles in the environment. *Environ. Sci. Technol.* **37,** 786–791.

Utsunomiya S., Peters S. C., Blum J. D., and Ewing R. C. (2003) Nanoscale mineralogy of arsenic in a region of New Hampshire with elevated As-concentrations in the groundwater. *Am. Mineral.* **88,** 1844–1852.

Wells J. D. and Mullens T. E. (1973) Gold-bearing arsenian pyrite determined by microprobe analysis, Cortez and Carlin Gold mines, Nevada. *Econ. Geol.* **68,** 187–201.

Widler A. M. and Seward T. M. (2002) The adsorption of gold (I) hydrosulphide complexes by iron sulphide surfaces. *Geochim. Cosmochim. Acta* **66,** 383–402.

Wu X. and Delbove F. (1989) Hydrothermal synthesis of gold-bearing arsenopyrite. *Econ. Geol.* **84,** 2029–2032.

Ye Z. (2001) Geological and geochemical controls on mineralization and alteration, Screamer Carlin-type gold deposit, Nevada. M.Sc. thesis, Univ. of Michigan, Ann Arbor.

Ye Z., Kesler S. E., Essene E. J., Zohar P. B., and Borhauer J. L. (2003) Relation of carlin-type gold mineralization to lithology, structure and alteration; Screamer Zone, Betze-Post Deposit, Nevada. *Mineral. Dep.* **38,** 22–38.

APPENDIX

Table A1. Secondary-ionization mass spectrometry (SIMS) analyses of Au and As in arsenian pyrite. Coarse: >50 μm; medium: 10–50 μm; fine: 2–10 μm; microcrystalline: <2 μm.

Deposit/Sample	Pyrite type	As (wt.%)	Au (ppm)	Deposit/Sample	Pyrite type	As (wt.%)	Au (ppm)
Lower Post	Coarse	1.00	0.41	Lower Post	Fine	3.89	175
HC-3086		0.02	0.25	HC-3086		4.36	303
		0.02	0.15			1.80	15
		0.01	0.17			2.38	12
		0.14	0.21			3.01	415
		0.21	0.14			1.84	16
		0.01	0.2			2.90	183
		0.07	0.15			1.96	23
		0.06	0.41			2.02	164
		0.13	0.22			4.21	375
		0.08	0.24			0.61	32
		0.06	1.2			4.04	131
		0.02	1.1			2.81	138
		0.14	30			3.66	16
		0.26	2.3			4.44	255
		0.15	0.22			5.15	226
		0.05	0.15			2.23	45
	Blastic	0.39	3.8			3.76	256
		0.01	0.29			2.56	219
		0.01	0.15			4.98	16
		0.03	7.6			1.27	18
		0.35	1.1			4.44	11
		0.03	0.5			2.13	17
		0.01	4.9			4.64	258
		0.80	0.44			2.70	3.5
		0.32	0.97			0.53	6.3
		0.68	0.95			0.29	31
		4.44	3.6			1.38	12
		0.30	0.43			3.71	468
		0.02	7.9			3.03	1.2
		0.05	0.21			2.60	132
		0.64	0.26			0.40	4.6
		0.86	0.81			1.50	15
		1.88	2			0.22	11
		1.26	31			0.11	0.7
		1.61	14			1.09	32
		0.01	0.64			0.36	11
		0.14	4.7			0.63	14
		0.09	0.19			0.44	2.6
		0.04	0.53			0.67	6.2
		0.18	0.6			1.37	75
		0.86	0.66			0.05	0.38
		0.01	0.5			0.40	2.8
		0.30	57			0.19	7.6
		0.33	9.5			0.34	1.8
		0.03	4.6			1.09	37
		0.25	1.3			0.10	2.7
		0.07	0.53		Microcrystalline	4.72	339
		0.01	0.31			6.15	555
		0.12	0.42			4.80	308
		0.01	3.5			5.61	293
		0.08	0.71			7.41	556
		1.05	0.42			4.64	165
		0.12	19			3.32	232
		3.95	0.41			4.16	276
						4.80	280

Appendix (Continued)

Deposit/Sample	Pyrite type	As (wt.%)	Au (ppm)	Deposit/Sample	Pyrite type	As (wt.%)	Au (ppm)
Lower Post	Microcrystalline	4.06	259	Lower Post	Framboidal	0.26	2.9
HC-3086	(cont.)	6.18	424	HC-3086		0.08	0.47
		6.80	283			0.92	323
		6.14	471			0.13	1.9
		6.40	529			0.26	4
		3.17	294			0.92	85
		4.00	271			1.77	259
		4.36	184			0.37	111
		5.29	220			0.28	37
		2.22	147			0.84	23
		4.08	286			0.16	4.2
		3.48	586			0.13	0.55
		6.14	407			0.28	1.2
		3.76	254			0.46	82
		3.34	277			0.19	21
		4.87	411			0.08	1.2
		4.50	405			0.08	0.55
		4.99	231			0.50	18
		4.71	330			0.32	13
		4.25	225			0.06	19
		4.45	187			0.31	22
		4.46	172			0.11	0.74
		3.05	242			0.20	7.1
		2.33	114			0.53	12
		3.62	96			0.09	1.5
		4.14	290			0.05	0.79
		1.77	19			0.20	2.8
		9.11	1112			0.11	2.9
		0.28	4.2			0.19	4
		1.74	154			0.37	9.5
		1.23	265			0.21	8.1
		0.31	12			0.39	99
		1.47	316			0.14	5.7
		2.57	2.6			0.11	1.8
		8.77	1344			0.12	9.4
		8.88	2392				
		3.42	118	Lower Post	Coarse	0.02	0.35
		0.67	3.7	S-3168		0.01	0.33
		7.74	1395			0.38	2.8
		0.98	17			0.02	2.3
		4.54	0.68			0.05	1.2
		2.14	24			0.04	5.2
		2.66	147			0.01	1
		2.18	16			0.01	0.32
		1.65	1.9		Blastic	0.25	1
		1.02	31			0.02	3
		1.65	0.6			0.38	2
		6.75	1528			0.27	92
		0.87	29			0.03	2.2
		0.89	19			0.06	2.6
		5.02	0.78			0.21	0.62
		13.43	742			0.24	1.1
		6.66	1729			0.03	0.69
		5.33	1			0.02	3.2
		0.31	15			0.01	0.9
		0.40	30			0.02	0.41

Appendix (Continued)

Deposit/Sample	Pyrite type	As (wt.%)	Au (ppm)	Deposit/Sample	Pyrite type	As (wt.%)	Au (ppm)
Lower Post	Blastic	0.01	0.53	Lower Post	Microcrystalline	4.58	247
S-3168	(cont.)	0.38	0.81	S-3168	(cont.)	4.76	726
		0.04	2.9			3.57	215
		0.41	31			5.00	223
		0.02	0.46			3.61	294
		0.02	4.8			5.30	237
		0.02	0.53			2.11	136
		0.06	3.2			3.68	76
		0.54	1.7			3.40	293
	Fine	0.18	81			6.40	187
		0.30	34			2.73	344
		0.09	21			3.66	103
		0.04	3				
		0.19	22	Mule Canyon	Coarse	0.61	1.7
		0.17	23	PP1		0.10	0.4
		0.25	8.9			0.01	0.8
		0.04	2.5			0.21	0.4
		0.08	20			0.01	0.5
		0.06	8.4		Medium	0.23	39.2
		0.04	5.6			0.04	2.2
		0.19	35			5.50	49.3
		0.16	8.6			0.01	1.2
		0.11	14			0.02	3.5
		0.27	1.6			0.47	14.2
		0.55	2.5		Fine	1.32	7.8
		0.07	3.3			0.01	0.8
		0.60	74			0.05	0.6
		0.38	66			0.01	0.5
		0.59	14			0.10	0.6
		0.37	105			0.05	8.7
		0.06	6.2			0.01	0.8
		0.16	13			1.32	7.8
		0.13	19		Framboidal	0.17	133.7
		0.25	28			0.07	11.4
		0.78	80			0.03	2.4
		1.01	239			1.51	22.3
		1.77	186			0.03	2.7
		0.79	168			0.02	1.2
		1.30	179			1.78	20.2
		0.09	11			3.40	9
		0.26	89			4.24	483.9
		0.11	6.7			0.20	43.9
	Microcrystalline	2.29	97			0.70	2.2
		1.97	171			0.29	8
		1.65	76			0.86	0.7
		3.72	29			0.12	6.3
		3.54	472			0.02	1.5
		3.94	6.6			0.80	67.8
		3.13	22			0.90	261.7
		4.25	222			0.17	133.7
		1.80	172			0.07	11.4
		4.89	144			0.03	2.4
		2.75	79			1.51	22.3
		4.23	206			0.03	2.7
		0.37	20			0.02	1.2
		2.40	74			1.78	20.2

Appendix (Continued)

Deposit/Sample	Pyrite type	As (wt.%)	Au (ppm)	Deposit/Sample	Pyrite type	As (wt.%)	Au (ppm)
Mule Canyon	Coarse	1.82	74.7	Kirazli	Framboidal	0.023	27
PP2		0.04	0.6	Turk-21		0.027	8
		0.34	1.8			0.034	32
		0.53	74.7			0.007	19
		1.04	6.1			0.003	12
		0.01	0.4			0.46	115
		0.07	0.6			0.42	105
		1.82	74.7			0.29	51
	Fine	2.44	33.3			0.08	16
		1.42	130.2			0.011	22
		0.10	3.7			0.003	33
		3.90	76			0.021	25
		0.02	2.9			0.008	27
		1.25	7.3			0.06	14
		1.09	64.8			0.2	51
		0.11	2.3			0.005	18
		0.01	5.6			0.035	18
		0.88	33.3			0.68	70
	Framboidal	0.88	11.3			0.028	13
		0.10	159			0.023	52
		0.22	28.3			0.007	17
		3.81	15.7			0.012	25
		1.54	37.9			0.013	25
		4.79	107			0.07	29
		1.85	5.9			0.3	22
		0.17	3			0.028	23
		0.78	142.1				
		0.02	4.5	Kirazli	Massive	0.49	9.2
		4.41	90.6	Turk-22		0.17	0.7
		3.44	25.3			0.14	0.6
		5.32	202.6			0.09	0.7
		2.18	180.5			0.09	1.3
		0.03	9.8			0.08	1
		0.03	1.7			0.014	5
		0.32	66			0.08	0.3
		0.40	6.7			0.12	1
		4.98	1691.1			0.70	0.8
		0.41	37.7			0.25	110
		0.34	33.4			0.063	0.6
		0.51	124.3			0.38	0.4
						0.18	0.5
						0.17	0.9
						0.11	0.4
						0.019	0.8
						0.006	0.3
						0.13	0.9
						0.62	13
						0.36	43
						0.17	0.4
						0.42	0.9